Doped hydrogenated nanocrystalline silicon oxide layers for high-efficiency c-Si heterojunction solar cells

Zhao, Yifeng; Mazzarella, Luana; Procel, Paul; Han, Can; Yang, Guangtao; Weeber, Arthur; Zeman, Miro; Isabella, Olindo

DOI
10.1002/pip.3256

Publication date
2020

Document Version
Final published version

Published in
Progress in Photovoltaics: research and applications

Citation (APA)
Zhao, Y., Mazzarella, L., Procel, P., Han, C., Yang, G., Weeber, A., Zeman, M., & Isabella, O. (2020). Doped hydrogenated nanocrystalline silicon oxide layers for high-efficiency c-Si heterojunction solar cells. *Progress in Photovoltaics: research and applications*, *28*(5), 425-435. https://doi.org/10.1002/pip.3256

Received: 8 November 2019 | Revised: 1 February 2020 | Accepted: 3 February 2020
DOI: 10.1002/pip.3256

RESEARCH ARTICLE

PROGRESS IN PHOTOVOLTAICS WILEY

Doped hydrogenated nanocrystalline silicon oxide layers for high-efficiency c-Si heterojunction solar cells

Yifeng Zhao[1] | Luana Mazzarella[1] | Paul Procel[1] | Can Han[1,2,3] | Guangtao Yang[1] | Arthur Weeber[1,4] | Miro Zeman[1] | Olindo Isabella[1]

[1] Photovoltaic Materials and Devices Group, Delft University of Technology, Delft, The Netherlands

[2] Institute of Photoelectronic Thin Film Devices and Technology, Nankai University, Tianjin, China

[3] Shenzhen Institute of Wide-Bandgap Semiconductors, Shenzhen, China

[4] ECN.TNO Solar Energy, Petten, The Netherlands

Correspondence
Yifeng Zhao, Photovoltaic Materials and Devices Group, Delft University of Technology, Mekelweg 4, 2628 CD, Delft, The Netherlands.
Email: y.zhao-4@tudelft.nl

Abstract

Hydrogenated nanocrystalline silicon oxide (nc-SiO_x:H) layers exhibit promising optoelectrical properties for carrier-selective-contacts in silicon heterojunction (SHJ) solar cells. However, achieving high conductivity while preserving crystalline silicon (c-Si) passivation quality is technologically challenging for growing thin layers (less than 20 nm) on the intrinsic hydrogenated amorphous silicon ((i)a-Si:H) layer. Here, we present an evaluation of different strategies to improve optoelectrical parameters of SHJ contact stacks founded on highly transparent nc-SiO_x:H layers. Using plasma-enhanced chemical vapor deposition, we firstly investigate the evolution of optoelectrical parameters by varying the main deposition conditions to achieve layers with refractive index below 2.2 and dark conductivity above 1.00 S/cm. Afterwards, we assess the electrical properties with the application of different surface treatments before and after doped layer deposition. Noticeably, we drastically improve the dark conductivity from 0.79 to 2.03 S/cm and 0.02 to 0.07 S/cm for n- and p-contact, respectively. We observe that interface treatments after (i)a-Si:H deposition not only induce prompt nucleation of nanocrystals but also improve c-Si passivation quality. Accordingly, we demonstrate fill factor improvement of 13.5%$_{abs}$ from 65.6% to 79.1% in front/back-contacted solar cells. We achieve conversion efficiency of 21.8% and 22.0% for front and rear junction configurations, respectively. The optical effectiveness of contact stacks based on nc-SiO_x:H is demonstrated by averagely 1.5 mA/cm^2 higher short-circuit current density thus nearly 1%$_{abs}$ higher cell efficiency as compared with the (n)a-Si:H.

KEYWORDS

silicon heterojunction (SHJ), hydrogenated nanocrystalline silicon oxide (nc-SiO_x:H), optoelectrical properties, interface treatments, carrier-selective-contacts (CSCs)

---

1 | INTRODUCTION

Silicon heterojunction (SHJ) solar cells demonstrated excellent efficiencies that are well beyond 25%,[1,2] and therefore becoming one of the most promising technology to reduce the levelized cost of electricity. The crucial ingredient to achieve such high efficiency is the incredibly high open-circuit voltage (V_{OC}), which is above 750 mV.[3-5] Typically, SHJ contact stack structures consist of intrinsic and doped a-Si:H thin layers (less than 15 nm) grown by plasma-enhanced chemical vapor deposition (PECVD). Theses Si cells with thin-film layers must also feature certain properties to build efficient contacts in terms of carrier selectivity and carrier selective transport for obtaining a high fill factor (*FF*).[6] Such layer properties point to minimal activation energy (E_a) for both contacts whereas wider bandgap (E_g) is more favorable for the collection of holes (p-contact).

Despite their limited thickness, a-Si:H–based thin films induce significant parasitic losses when placed on the sunny side of the cell.[7] Besides, E_a of doped a-Si:H layers is in the order of hundreds of meV because of their moderate doping efficiency.[8] The attempt of reaching higher doping within a-Si:H films increases defect density, which will deteriorate the effective carrier collection.[9] To quench this material bottleneck and owing to their superior electrical and favorable optical properties, hydrogenated nanocrystalline silicon (nc-Si:H) layers have been proposed for carrier-selective-contacts (CSCs) in SHJ solar cells.[10-13] The material consists of small nanocrystals embedded in the amorphous matrix,[14] giving confirmed anisotropy properties in the growth direction.[15] Furthermore, nc-Si:H alloyed with oxygen (nc-SiO_x:H) allows tunable optoelectrical properties,[16,17] with the advantage of simultaneously obtaining higher E_g and lower E_a, when compared with a-Si:H. This unique feature also enables more flexibility to tailor the selective transport for enhancing solar cells performance.[6] Interestingly, with similar optical transparency, n-type nc-SiO_x:H layers exhibit generally higher conductivity than p-type layers.[18,19] Accordingly, the use of p-type nc-SiO_x:H as a front emitter in SHJ cell, which demands a more sensitive processing than n-type counterpart, is rarely reported.[20-22]

On the other hand, in SHJ solar cell application, it is challenging to maintain an excellent electrical cell performance while optimizing the optical layer properties because of the substrate growth selectivity on top of the (i)a-Si:H layer.[23] Research and development have been devoted in studying the interface treatment to properly grow a nanocrystalline structure.[24-28] In particular, hydrogen plasma treatment (HPT) is widely studied for improving the c-Si/(i)a-Si:H chemical interface-passivation quality.[29,30] From Si thin-film experience, this treatment can also result in a low-temperature crystallization of a-Si[31] that might be beneficial for nanocrystal growth. Aside from HPT, non-oxidic seed layer[26,27] and CO_2 plasma treatments[28] are also utilized to minimize the incubation layer thickness on thin nc-Si:H layers. It is also well known that very-high-frequency (VHF) plasma may induce less ion bombardment compared with radio-frequency (RF)[32] and thus, it is more efficient for reaching higher crystallinity fraction (F_C) within thin layers.[33] Therefore, it is critical to explore nucleation methods for achieving excellent bulk conductivity and nanocrystal growth of thin (less than 20 nm)doped nc-SiO_x:H layers while maintaining excellent passivation quality. In this contribution, we explore highly transparent selective transport layers for carrier collection based on nc-SiO_x:H for SHJ solar cells. After the section about experimental details, the remainder of this paper is organized as follows: first, we study the optoelectrical properties of doped nc-SiO_x:H layers by varying PECVD deposition parameters. Afterwards, we investigate the effects of different interface treatments in both n-type and p-type contact stacks. Finally, we discuss the impact of the interface treatments into front/back-contacted silicon heterojunction solar cells.

2 | EXPERIMENTAL DETAILS

For layer optimization, both n-type and p-type nc-SiO_x:H layers are deposited on Corning Eagle XG glass using radio-frequency (RF, 13.56 MHZ) multichamber PECVD system with thicknesses from 40 to 100 nm. The PECVD parameters are presented in Table 1. Layer thicknesses are found by modeling measured spectroscopic ellipsometry (SE) spectra with the effective-medium approximation (EMA) Bruggeman model.[34] A temperature-dependent I-V setup is used, whose probes touch aluminum strips evaporated on the layers in

TABLE 1 PECVD parameters for optimization of doped nc-SiO_x:H layers, doped nc-Si:H, pre-HPT, VHF (i) nc-Si:H treatment, post-HPT, and (n)a-Si:H

PECVD Parameters	(n) nc-SiO_x:H	(p) nc-SiO_x:H	(n) nc-Si:H	(p) nc-Si:H	pre-HPT	VHF (i) nc-Si:H	post-HPT	(n) a-Si:H	(p) a-Si:H
Frequency (MHz)	13.56	13.56	13.56	13.56	13.56	40.68	13.56	13.56	13.56
Temperature (°C)	180	180	180	180	180	180	180	180	180
Pressure (mbar)	1.1-4.4	1.4-3	2.7	2.2	2.7/2.2	4	2.7	0.6	0.9
Power (mW/cm^2)	55-90	55-90	76	90	63	69	21	28	16
SiH_4 (sccm)	1	0.8	1	0.8	/	1.2	/	40	8
H_2 (sccm)	60-160	110-210	100	170	200	120	200	/	24
CO_2 (sccm)	0-2.2	0-2.8	0	0	/	/	/	/	/
PH_3 or B_2H_6 (200 ppm in H_2) (sccm)	0.7-3.7	/	1.2	/	/	/	/	11	8
B_2H_6 (200 ppm in H_2) (sccm)	/	5-30	/	10	/	/	/	/	/

order to measure lateral dark conductivity (σ_d) and E_a of deposited layers. The real part of the refractive index (n) and the E_{04}, which is the energy at which the absorption coefficient reaches 10^4 1/cm, are obtained by fitting a thin-film multilayer model in SCOUT software[35] with measured reflectance and transmittance spectra. F_C is extracted by Raman spectroscopy with a green laser (λ_{laser} = 514 nm), using a fitting model similar as used in Tan et al.[34] However, the existence of nanocrystals is hardly distinguishable when fitted F_C is below 25%. We analyze the composition of the hydrogen bonding configurations and microstructure of the (i)a-Si:H layer by Fourier-transform infrared (FTIR) spectroscopy.

For solar cell preparation, we use a 4-inch Topsil n-type double-side polished float-zone (FZ) < 100 > c-Si wafers with resistivity of 3 ± 2 Ω cm and thickness of 280 ± 20 μm. The wafers are double-side textured in TMAH solution with ALKA-TEX as additive.[36] Subsequently, they are cleaned through a wet chemical oxidation process using nitric acid (HNO_3) and afterward dipped into 0.55% HF for 5 minutes immediately before being loaded into the PECVD equipment.[37] The deposition time is adapted for tilted pyramids using the geometrical factor[38] of 1.7. Firstly, one side of the c-Si wafer is passivated with (i)a-Si:H/n-type contact stack to form the electron contact. Afterwards, (i)a-Si:H/p-type contact stack is deposited on the other side of the wafer to form the hole contact. To investigate the effect of nucleation on the growth of doped layers, the deposition of non-oxidic–doped nc-Si:H, pre-HPT, and/or VHF (i)nc-Si:H treatments are applied right after the (i)a-Si:H deposition. After contact stack deposition, post-HPT and doped a-Si:H capping layer are additionally applied (see Table 1). Besides, the indium tin oxide (ITO) is sputtered on both front and rear sides of the solar cell precursors with thickness of 75 and 120 nm, respectively. Lastly, screen printed Ag paste is applied and cured in an oven under air atmosphere at a temperature of 170°C for 45 minutes for each side. Unless specifically mentioned, solar cells fabricated in this study have an area of 7.84 cm^2 with 12.5% metal coverage.

The passivation quality of solar cell precursors is measured by Sinton WCT-120 under transient photo-conductance decay (transient PCD) mode. The current-voltage characteristics under illumination of solar cells are tested with an AAA class Wacom WXS-156S-L2 solar simulator under standard test conditions (STC) and using a calibrated reference solar cell. In-house external quantum efficiency (EQE) setup is used to obtain the integrated $J_{SC,EQE}$ for analyzing the spectral response without the influence of the front metal grid. We use Sinton Suns-VOC-150 Illumination-Voltage Tester to acquire the pseudo *FF* (*pFF*).

3 | RESULTS AND DISCUSSIONS

3.1 | Tunable optoelectrical properties of doped nc-SiO_x:H

To evaluate the optimal trade-off of optoelectrical parameters of doped nc-SiO_x:H for solar cell applications, we performed a series of experiments varying the PECVD process parameters (see Table 1). The summary of measured n, σ_{dark}, and E_{04}, E_a, and F_C of doped nc-SiO_x:H, nc-Si:H, and a-SiO_x:H layers within the explored PECVD process window is illustrated in Figure 1.

As shown in Figure 1A, we firstly address the trade-off between optical and electrical properties of doped nc-SiO_x:H layers. For n-type layers, along with the increment of n, the improvement of σ_{dark} is generally observed, which indicates lower fraction[39] of (n) a-SiO_x:H but more conductive (n)nc-Si:H and/or (n)a-Si:H phase

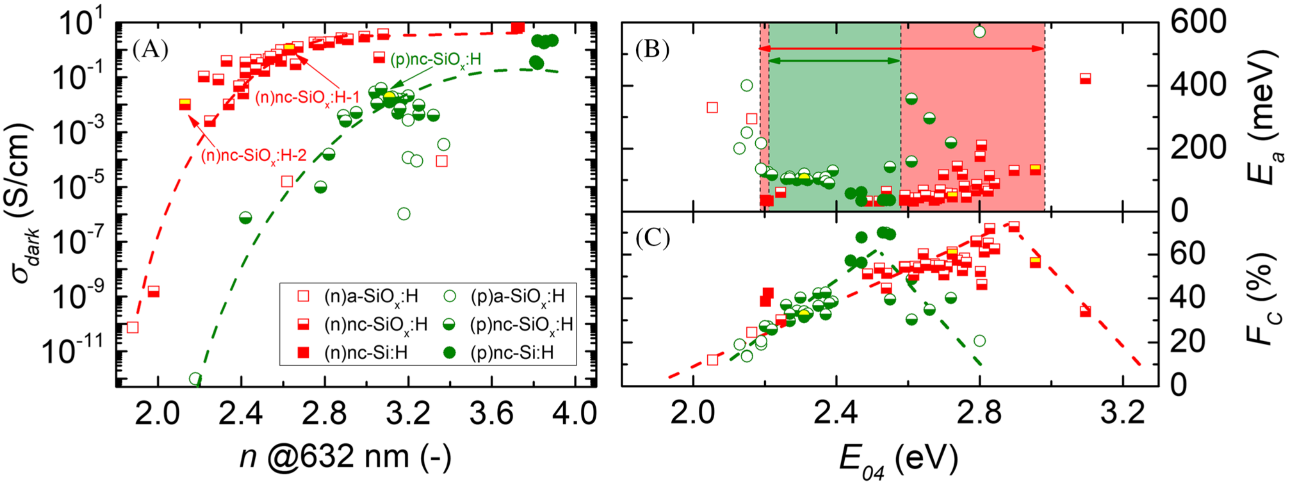

FIGURE 1 The sum-up of measured optoelectrical properties of doped nc-SiO_x:H, nc-Si:H, and a-SiO_x:H layers during the optimization process: (A) σ_{dark} vs n; (B) E_a vs E_{04}; (C) F_C vs E_{04}. Note: half-down symbols represent nc-SiO_x:H layers; solid symbols represent nc-Si:H layers that miss CO_2 during the depositions; open symbols that distinguish a-SiO_x:H are based on F_C from Raman spectroscopy; dashed lines in A,C are guides to the eye; colored rectangular areas in B indicate the optical window of achieving acceptable E_a (less than 200 meV) for solar cells application. Doped nc-SiO_x:H layers that are used in fabricating solar cells are marked with labels given in Table 2 [Colour figure can be viewed at wileyonlinelibrary.com]

inside the material. To be more specific, increasing the deposition pressure and decreasing deposition power result in layers feature larger *n*, and these are also observed by Gabriel et al who ascribe the increasing of *n* with decreased "power to pressure ratio" to less incorporation of oxygen in the mixed-phase material.[40] Besides, changing directly the composition of precursor gases, mainly decreasing H_2 flow and CO_2 flow, results in higher *n* as well, and this is observed in literature.[39-42] However, the nanocrystalline phase is hardly seen when depositions feature insufficient H_2 dilution (less than or equal to 60 sccm) or inappropriate pressure (less than or equal to 1.1 mbar and greater than or equal to 4.4 mbar) (see (n)a-SiO$_x$:H in Figure 1A). Indeed, nucleation of nc-Si requires sufficient atomic hydrogen in the plasma, while this is not likely to happen when H_2 dilution is too low and deposition pressure is too high.[41,43,44]

As for p-type layers, changes of deposition conditions induced the increased *n* of p-type layers may be explained similarly as that of n-type layers. The increased *n* is mainly seen by increasing deposition pressure, B_2H_6 flow and decreasing deposition power, H_2 flow and CO_2 flow. The (p)a-SiO$_x$:H shown in Figure 1A is due to high CO_2 flow (greater than 2.8 sccm), high B_2H_6 flow (greater than 25 sccm), low H_2 flow (less than 130 sccm), or high pressure (greater than 3 mbar). The amorphization induced by the high B_2H_6 flow could be related to a similar finding reported in Cuony et al,[45] where a monotonic decrement of F_C is observed with increased TMB/SiH_4 ratio. Moreover, for both n- and p-type layers, highly conductive nc-Si:H layers are obtained when CO_2 is missing during the deposition.

Moreover, as shown in Figure 1B, n-type layers exhibit a wider optical window to achieve acceptable E_a for solar cell application as compared with p-type layers. Therefore, front surface field (FSF) featuring (n)nc-SiO$_x$:H is supposed to be a better candidate and easier to apply in solar cells than (p)nc-SiO$_x$:H. Lastly, as shown in Figure 1C, the variation of extracted F_C with E_{04} reflects the change of constituents of this mixed-phase material. The positive correlation between F_C and E_{04} of doped nc-SiO$_x$:H is mainly due to more hydrogen and/or more oxygen incorporation into the layer,[41] while the atomic hydrogen-induced nucleation effect can still compensate the amorphization effect from oxygen. However, when oxygen incorporation exceeds a certain limit, the nanocrystal growth is compromised as discussed in literatures.[34,39,41,45]

Overall, tunable optoelectrical properties of doped nc-SiO$_x$:H layers enable the flexibility to tailor the selective transport[6] for enhancing solar cells performance. In Table 2, we report the optimized optoelectrical properties of both p-type and n-type nc-SiO$_x$:H layers for subsequent solar cell applications.

3.2 | Interfaces treatments on doped contact stacks

In this section, we evaluate the variations in doped layers properties for different interface treatments: (a) after (i)a-Si:H deposition (pre-treatment) and (b) after doped layer deposition (post-treatment). To accelerate the nucleation of nc-SiO$_x$:H, we introduced pre-treatments including pre-HPT, VHF (i)nc-Si:H treatment and the application of a non-oxidic (n)nc-Si:H or (p)nc-Si:H seed layer just before the n-type and p-type type contact stack deposition, respectively. Post-treatments such as (n)a-Si:H or (p)a-Si:H capping layer after the growth of the contact stacks were tested. Additionally, we also applied a post-HPT after n-type contact stack deposition. Figure 2A,B shows the schematic illustration of treatments applied on n-type and p-type contact stack, respectively.

Therefore, we coated glass samples with 10-nm thick (i)a-Si:H followed by n-type contact stack ((n)nc-SiO$_x$:H–1 + (n)nc-Si:H) or p-type contact stack ((p)nc-SiO$_x$:H + (p)nc-Si:H). Subsequently, we characterized the doped contact stack's electrical properties in terms of E_a and σ_{dark}. Figure 3 illustrates the effects of pre- and post-treatments on doped layers, whereas those treatments were already firstly optimized in terms of plasma conditions and deposition time to have better electrical properties of doped layers without negatively affecting the passivation quality in solar cell application. In Figure 3A, the combined treatment-1 represents: pre-HPT + (n)nc-Si:H seed + n-type contact stacks + post-HPT + (n)a-Si:H, while combined treatments-2 represents: pre-HPT + VHF (i)nc-Si:H seed + n-type contact stacks + post-HPT + (n)a-Si:H.

Considering samples without any treatment indicated as the reference, for n-type contact stack, layers exposed to single pre-treatment and post-treatment exhibit decrements of E_a. Especially, for the single treatments, the use of (n)a-Si:H capping layer plays the most significant role for improving E_a from 53.5 to 36.5 meV and doubling σ_{dark} from 0.79 to 1.57 S/cm. Such an effect evidences that (n)a-Si:H performs a better interface contact with metal than (n)nc-Si:H counterpart. Note that the (n)a-Si:H we used in this experiment was previously optimized with E_a of 206 meV and σ_{dark} of 0.02 S/cm. Faster nucleation is seen by applying pre-HPT, non-oxidic (n)nc-Si:H, and VHF (i)nc-Si:H treatment, which increase σ_{dark} as compared with the reference sample. However, it is worth noting that contact stack after the 20-minutes post-HPT treatment exhibits slightly reduced lateral σ_{dark} than the reference sample. Since the lateral σ_{dark} is measured by probing contacts which are formed on the surface of the layer, the reduction of lateral σ_{dark} indicates that the surface of the contact stack is less laterally conductive after post-HPT. We speculate that surface amorphization (few nanometers) is induced by this low-power post-

TABLE 2 Optoelectrical properties of selected nc-SiO$_x$:H layers

Layers	Thickness (nm)	σ_{dark} (S/cm)	E_a (meV)	E_{04} (eV)	n @ 632 nm (–)	F_C (%)
(n)nc-SiO$_x$:H-1	63.4	1.02	46.6	2.72	2.63	60.1
(n)nc-SiO$_x$:H-2	50.3	0.01	132.1	2.96	2.13	56.3
(p)nc-SiO$_x$:H	68.7	0.02	103.6	2.31	3.11	32.3

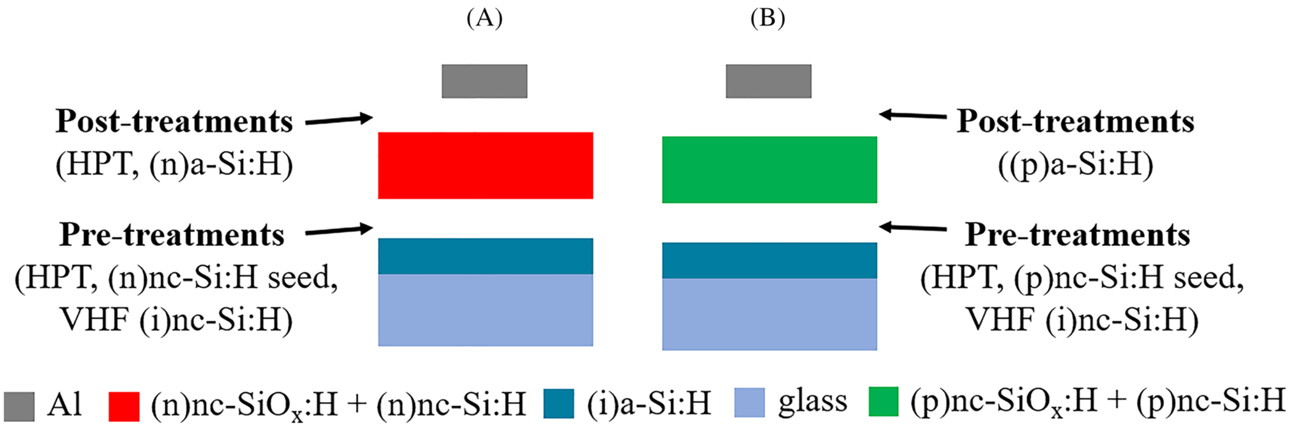

FIGURE 2 Schematic illustration of treatments applied on (A) n-type and (B) p-type contact stack, respectively [Colour figure can be viewed at wileyonlinelibrary.com]

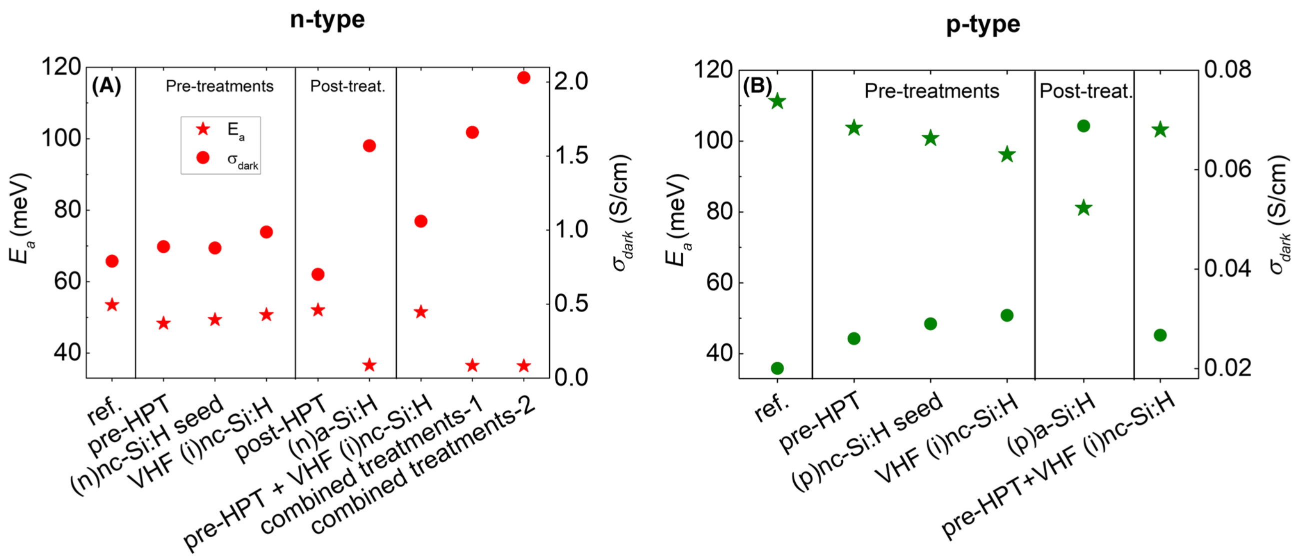

FIGURE 3 Measured electrical properties (E_a and σ_{dark}) of (A) n-type and (B) p-type contact stacks with different pre- or post-treatments. The total thickness of the doped contact stack is 82 ± 2 nm [Colour figure can be viewed at wileyonlinelibrary.com]

HPT leading to a low conductivity amorphous film. Nevertheless, we cannot detect such shallow-surface F_C changes as compared with the thick bulk layer. This is because of the Raman spectroscopy used in this study, which features a penetration depth in the range of hundred nanometers. HPT-induced amorphization of nc-Si:H is reported,[46] for which a layer with initial F_C over 20% (with the existence of grain boundaries) experiences a decrease of F_C after HPT, resulting from migrating H atoms that minimize lattice strain energy. As reported elsewhere,[47] the formation of a few nanometers disordered surface layer on p-type CZ-Si after HPT is confirmed by cross-sectional transmission electron microscopy (TEM). In any case, by means of SE, we observe no etching of the contact stack after the post-HPT. By combining the applied pre- and post-treatments, we are able to improve further the σ_{dark} of the n-type contact stacks from 0.79 to 2.03 S/cm as compared with the reference sample.

For p-type contact stack, we note positive effects in applying pre-treatments in terms of lower E_a and higher σ_{dark}. Among pre-treatments, the most obvious enhancement of E_a (from 111.2 to 96.4 meV) and σ_{dark} (from 0.02 to 0.03 S/cm) is seen when applying VHF (i)nc-Si:H treatment after (i)a-Si:H deposition. The VHF plasma conditions used in this study are acting mainly as surface treatment, since no change in thickness is detected by SE, even after 6 minutes of deposition. Similar to that of n-type contact stacks, we boost the σ_{dark} to 0.07 S/cm and reduce E_a to 81.1 meV by adding a (p)a-Si:H layer on p-type contact stacks. Moreover, we also observe improved electrical properties by combining the pre-HPT and VHF (i)nc-Si:H treatment as compared with the reference sample, while the combined treatments do not outperform samples with the corresponding single treatments.

To further understand the effects of pre-HPT and VHF (i)nc-Si:H treatment on the thin (i)a-Si:H layer, we evaluated the passivation quality and layer's microstructure. To this purpose, we prepared double-side textured symmetrical samples with 10-nm thick (i)a-Si:H and monitor the effective lifetime (τ_{eff}) and the structural change in

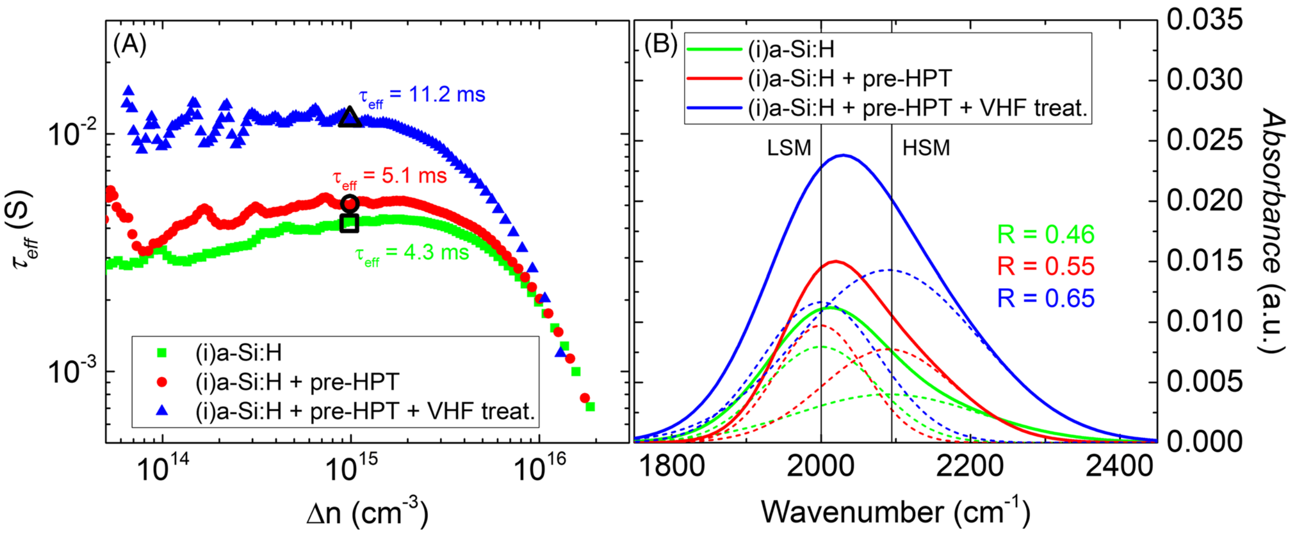

FIGURE 4 (A) Injection level dependent lifetime curve measured on symmetrical samples and (B) Fourier-transform infrared (FTIR) spectra in the range of 1700 to 2500 cm^{-1}, related to (i)a-Si:H samples without treatment, with HPT and with HPT + VHF (i)nc-Si:H treatment [Colour figure can be viewed at wileyonlinelibrary.com]

the layer because of the abovementioned treatments by measuring their FTIR spectra. Figure 4 depicts the injection level dependent τ_{eff} and the FTIR spectra related to the (i)a-Si:H without treatment (reference), with pre-HPT and with pre-HPT + VHF treatment.

As shown in Figure 4A, the reference sample without treatment demonstrates τ_{eff} values slightly over 4 ms (at Δn = 10^{15} cm^{-3}), while we observe improved passivation quality (τ_{eff} over 5 ms) when HPT is applied after the deposition of (i)a-Si:H. Interestingly, applying HPT + VHF (i)nc-Si:H treatment, we observe the most significant τ_{eff} enhancement resulting in values beyond 11 ms.

To investigate the reason for this improvement, we report in Figure 4B the corresponding FTIR spectra measured on the same samples. Results reveal the changes in hydrogen content and microstructure of (i)a-Si:H layer. The absorption peak can be deconvoluted into two Gaussian distributions, which are related to the low stretching mode (LSM) and high stretching mode (HSM) of Si—H bonds. It is well-established that LSM is assigned to monohydrides,[48] while HSM is attributed to dihydrides[49] or integrated clustered monohydrides groups at internal void surfaces.[48] The microstructure factor *R*, which combines both stretching modes to describe the layer quality, is defined as[50]:

$$R = I_{HSM}/(I_{HSM}+I_{LSM}) = I_{2090}/(I_{2090}+I_{2000}),$$

where I_{2090} (I_{HSM}) and I_{2000} (I_{LSM}) are integrated absorptions of Gaussian peaks at 2090 and 2000 cm^{-1}, respectively. As shown in Figure 4B, compared with the reference sample, we observe overall increased absorbance when either only HPT or combined treatments are applied. This indicates the overall increase of Si—H bonds inside the (i)a-Si:H,[29] which result in better passivation. Besides, the *R* increases when both only HPT and combined treatments are applied, thus revealing the reduced compactness of the (i)a-Si:H layer with those treatments. In other words, it indicates that the (i)a-Si:H is more close to the amorphous-to-crystalline transition region,[51] which can foster more effectively the nucleation of doped layers. Such an effect should be more noticeable especially when doped layers have thinner thickness.

To sum up, the applied pre-treatments on both n-type and p-type contact stacks demonstrate enhanced electrical properties for the test structures. Meanwhile, the combination of pre-HPT and VHF (i)nc-Si:H treatment is found to significantly improve the c-Si/(i)a-Si:H interface passivation quality. As for post-treatments, boosts of σ_{dark} are observed when doped a-Si:H capping layers are applied on the corresponding doped contact stacks. In the following, we investigated the effects of the aforementioned treatments on the performance of solar cell structures.

3.3 | Solar cells

Solar cells are fabricated using the n-type and p-type contact stacks discussed in Figure 3. In order to evaluate both optically and electrically the aforementioned layers on solar cells, we located the contact stack under study in front of the device. Therefore, we analyze n-type (p-type) contact in rear (front) junction devices. The schematic illustrations of reference cells' structures for treatments applied on n- and p-type contact stacks are shown in Figure 5. Besides the various treatments herein analyzed, the stacks under study closely follow the sort of contact stack that potentially optimizes carriers transport across heterointerfaces in SHJ cells.[6] In a nutshell, such optimal stack comprises (a) an (i)a-Si:H to achieve excellent surface passivation, (b) a high bandgap silicon-alloy layer (eg, nc-SiO_x:H) to induce stronger band banding at c-Si/(i)a-Si:H, and (c) a low bandgap silicon layer (eg, nc-Si:H) to enable efficient charge exchange with the TCO.

For n-type contact layers evaluation, the rear side p-type contact stack structure remains constant as (i)a-Si (8 nm)/(p)nc-SiO_x:H

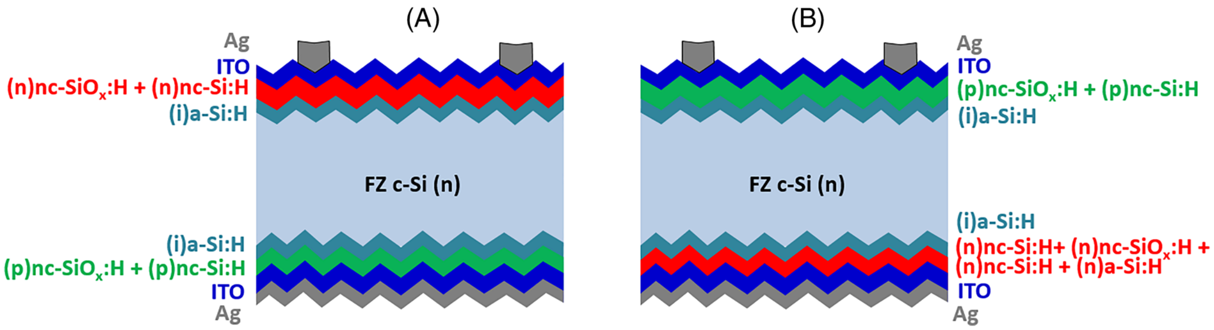

FIGURE 5 Schematic illustrations of reference cells' structures for studying effects of treatments applied on (A) n-type contact stack and (B) p-type contact stack [Colour figure can be viewed at wileyonlinelibrary.com]

(10 nm)/(p)nc-Si:H (10 nm), with reference n-type contact stack as (i) a-Si (8 nm)/(n)nc-SiO$_x$:H–1 (12 nm)/(n)nc-Si:H (3 nm) (see Figure 5A). Figure 6 illustrates solar cells' external parameters for different treatment conditions.

As shown in Figure 6, the reference cell shows *FF* of 65.6%, V_{OC} of 723 mV, $J_{SC,EQE}$ of 38.5 mA/cm^2, and η_{active} of 18.3%. When pre-HPT is applied, we measured improved EQE response, which is related to bandgap widening inside (i)a-Si:H with H incorporation that improves the short wavelength response.[30] However, cell with only pre-HPT exhibits a drastic *FF* drop of over 10%$_{abs}$ as compared with the reference cell. Such an effect could be ascribed to unexpected changes on contact properties of (n)nc-Si:H/ITO interface, even though further investigation is necessary. Indeed, while *FF* drop is induced by pre-HPT, it can be totally recovered and even improved when we additionally applied a post-HPT or with an extra (n)a-Si:H capping layer. Among these solutions, (n)a-Si:H is more beneficial with a *FF* gain of 6.3%$_{abs}$ as compared with the reference cell. Such an effect is consistent with results discussed in Section 2, where the (n)a-Si:H capping layer exhibits lower E_a and higher σ_{dark} values when (n)a-Si:H is in contact with the metal. However, in solar cells, n-type contact stack is in contact with sputtered ITO instead of metal; thus the gain of *FF* by applying (n)a-Si:H capping layer may result from different mechanisms as compared with the sample shown in Section 2. Nevertheless, a study of the n-type layer/ITO interface[52] using X-ray photoelectron spectroscopy (XPS) depth profiling measurements showed that (n)a-Si:H forms better interface with sputtered ITO as compared with (n)nc-Si:H. This is because of (a) the lack of oxygen segregation, (b) much less oxidized Si atoms near interface region, and (c) less ITO diffusion into (n)a-Si:H layer, while highly oxidized interface and ITO in-diffusion happens when (n)nc-Si:H is applied.[52] Besides, the formation of a-SiO$_x$:H(In) in ITO/(n)-Si interface during sputtering of ITO, which builds a potential barrier (ie, blocking the transport of electron), is also reported.[53] Those studies may explain the gain of *FF* by applying the (n)a-Si:H capping layer before ITO sputtering. Similarly, the possible shallow surface amorphization of contact stack result from the post-HPT as discussed in Section 2 may explain the improved *FF* of the solar cell, because amorphous layers relax the sharp potential change at TCO hetero-interfaces thus improving energy band alignment.[54] Nevertheless, the highly absorptive (n)a-Si:H induces an overall degradation of the $J_{SC,EQE}$ to below 38 mA/cm^2. The insertion of a 2-nm thick (n)nc-Si:H seed layer in combination with pre- and post-HPT provides a tiny *FF* improvement (0.4%$_{abs}$) but with a passivation degradation of 6 mV as compared with the cell with only pre- and post-HPT. The little gain of FF results from better doped contact stack owing to faster nucleation induced by non-oxidic doped layer,[26,27] while drop of V_{OC} is because of a rather aggressive deposition of (n)nc-Si:H directly on (i)a-Si:H layer. Eventually, solar cell with combined treatments-1, namely, pre-HPT + (n)nc-Si:H seed + n-type contact stacks + post-HPT + (n)a-Si:H, exhibits a 7.6%$_{abs.}$ of *FF* improvement relative to the reference cell.

Similarly, we investigate the effect of different treatments for p-type contact stack in front junction solar cells as shown in Figure 7. We kept the optimized strategy of n-type contact stack discussed in Figure 6 for all cells unless otherwise mentioned. The p-type contact stack has the following reference structure (i)a-Si (8 nm)/(p)nc-SiO$_x$:H (10 nm)/(p)nc-Si:H (10 nm) as reported in Figure 5B.

As illustrated in Figure 7, compared with the reference cell, different single pre-treatments: pre-HPT, (p)nc-Si:H seed layer, and the VHF (i)nc-Si:H treatment can improve the *FF* without deteriorating V_{OC} which remains above 720 mV. It is worth noting that VHF (i)nc-Si:H treatment and (p)a-Si:H capping layer demonstrate to be effective single treatments for improvement on *FF* of 2.2%$_{abs}$ from 72.1% to 74.3%. The *FF* improvement corresponds to observed σ_{dark} and E_a enhancements reported in Figure 3. However, (p)a-Si:H that is highly parasitic absorptive degrades the $J_{SC,EQE}$ from 37.0 to 35.2 mA/cm^2. Therefore, there is no gain in η_{active} by applying the (p)a-Si:H capping layer. Lastly, we combined pre-HPT and VHF (i)nc-Si:H treatment. Together with further thicknesses optimizations of contact stacks, we were able to obtain cell with overall improved V_{OC} from 721 to 723 mV, $J_{SC,EQE}$ from 37.0 to 37.8 mA/cm^2, *FF* from 72.1% to 76.9%, and η_{active} from 19.2% to 21.0% compared with the reference sample. The gain of performance is expected, as discussed in Figure 4, since (i) a-Si:H layer, after the combined treatments, tends to prompt the nucleation of nanocrystal growth on top while providing excellent passivation quality to c-Si/(i)a-Si:H interface.

In return, as inspired by the optimized pre-HPT and VHF (i)nc-Si:H treatment for p-type contact stack, these combined treatments are also investigated on n-type contact stack as pre-treatments in solar

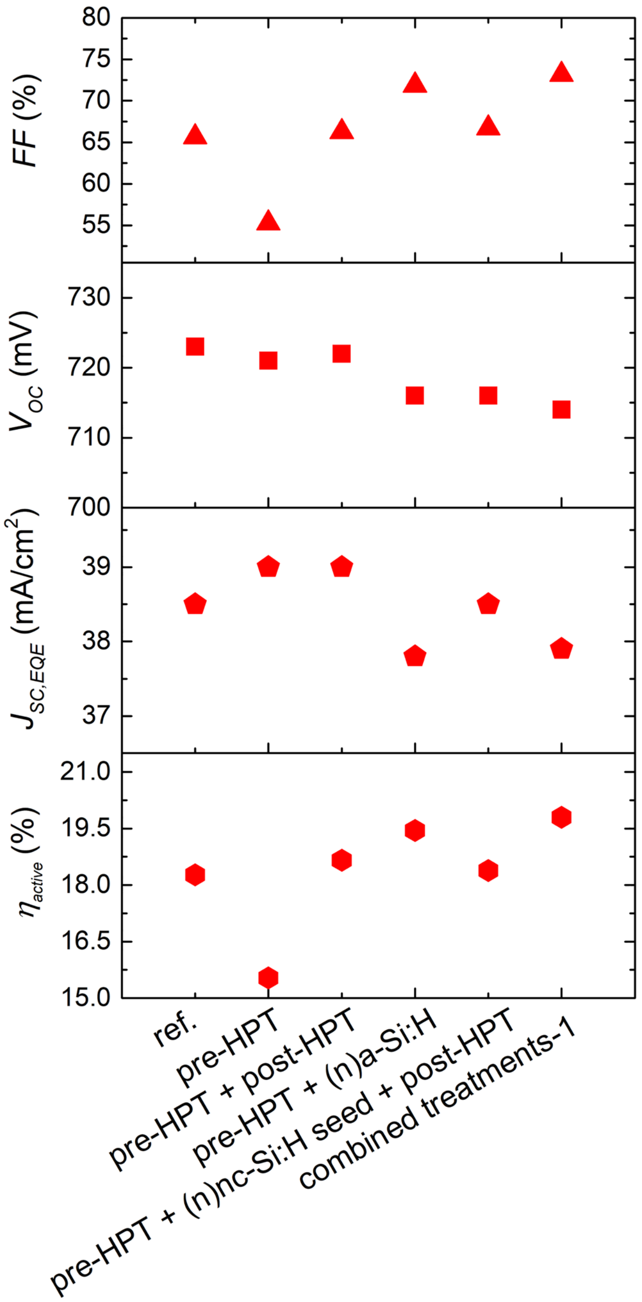

FIGURE 6 The solar cells' parameters for different treatments on n-type contact stack in rear junction structure. Combined treatments-1 represents pre-HPT + (n)nc-Si:H seed + n-type contact stacks + post-HPT + (n)a-Si:H. Each data point represents one solar cell [Colour figure can be viewed at wileyonlinelibrary.com]

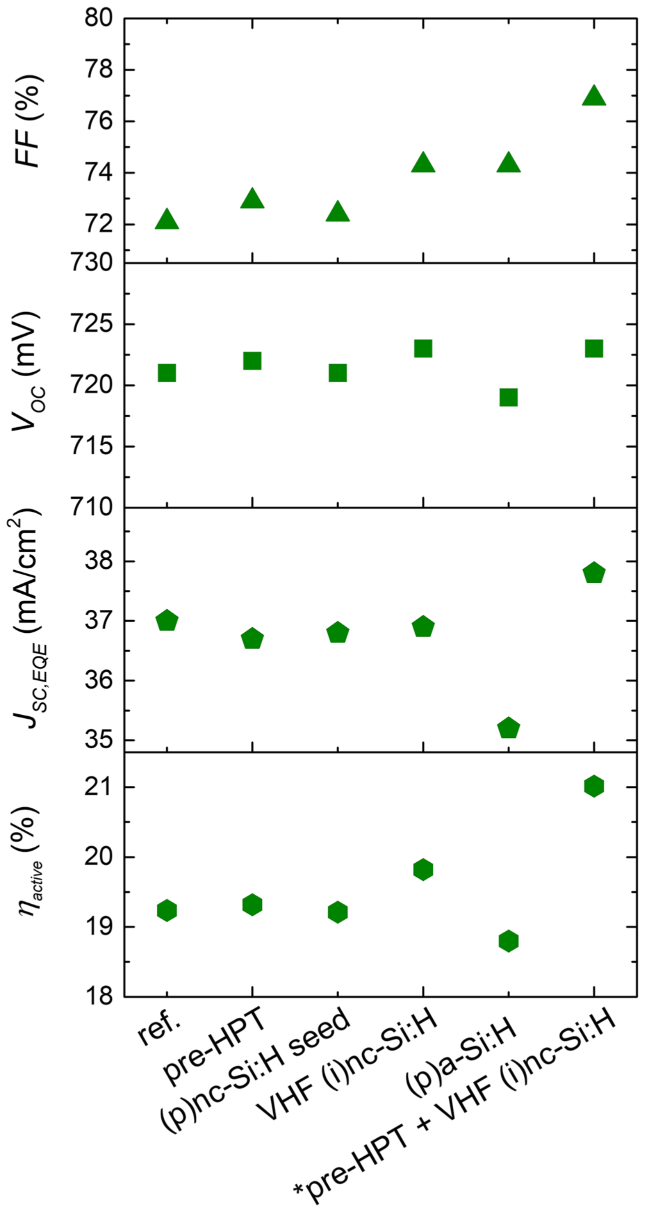

FIGURE 7 The solar cells' parameters with different treatments on p-type contact stack in front junction structure. *: cell features optimized thicknesses of both sides (i)a-Si:H and rear side (n)nc-SiO$_x$:H. Each data point represents one solar cell [Colour figure can be viewed at wileyonlinelibrary.com]

cells. As known from Figure 3A, we are able to observe improved σ_{dark} of n-type contact stack when the combined treatments-2 is applied as compared with combined treatments-1. However, precursor passivation quality is hardly preserved with direct application of (n)nc-SiO$_x$:H-1 layer after the pre-HPT and VHF (i)nc-Si:H treatment. Despite the optical advantage from (n)nc-SiO$_x$:H-2 (see Table 2), it also exhibits better preserved precursor passivation quality when pre-HPT + VHF (i)nc-Si:H treatments are applied with even thinner (i)a-Si:H layer beneath. Therefore, together with optimized p-type contact stacks, we use combined treatment-2 with (n)nc-SiO$_x$:H-2 for rear junction cells and combined treatment-1 with (n)nc-SiO$_x$:H-1 for front junction cells, respectively. The best front and rear junction cells with 7.84 cm^2 cell area are listed in Table 3 (cells 1 and 2). This 7.84-cm^2 cell design has a 12.5% metal coverage, which limits the measured J_{SC} below 34.0 mA/cm^2. A new cell design with 3.92-cm^2 wide area featuring 4.4% metal coverage has been then realized. With the new cell design and further fine-tuning contact stacks' thicknesses and treatments, more performant solar cells are obtained (see Table 3, cells 3 and 4).

Thanks to the highly transparent n-type nc-SiO$_x$:H layer that has a high E_{04} nearly 3.0 eV and low n of 2.13, at least 0.7 mA/cm^2 higher

TABLE 3 The illuminated J-V characterizations and pseudo parameters of the best solar cells

Cell Number	Cell Area (cm^2)	Metal Coverage (%)	Junction Position	V_{OC} (mV)	J_{SC} (mA/cm^2)	*FF* (%)	*η*, (%)	*pFF* (%)
1	7.84	12.5	Front	718	32.9	77.9	18.4	81.0
2	7.84	12.5	Rear[1]	714	34.0	75.3	18.3	81.5
3	3.92	4.4	Front	714	38.6	79.1	21.8	83.6
4	3.92	4.4	Rear[1]	712	39.3	78.6	22.0	83.9

[a] (n)nc-SiO$_x$:H-2 layer is chosen.

TABLE 4 The illuminated J-V parameters of rear-junction solar cells using different front n-type contacts. Results are averaged from three similar cells

n-Type Contacts	Cell Area, (cm^2)	Metal Coverage (%)	Junction Position	V_{OC} (mV)	J_{SC} (mA/cm^2)	*FF* (%)	*η* (%)
(n)nc-SiO$_x$:H layer stack[a]	3.92	4.4	Rear	713.3 ± 1.2	38.9 ± 0.5	79.0 ± 0.3	21.9 ± 0.2
(n)a-Si:H	3.92	4.4	Rear	712 ± 1.0	37.4 ± 0.3	79.4 ± 0.2	21.1 ± 0.2

[a] (n)nc-SiO$_x$:H-2 layer is chosen.

J_{SC} values are obtained for rear junction cells as compared with front junction cells (cell 2 vs cell 1 and cell 4 vs cell 3). Still, the higher *FF* achieved in front junction configuration yields similar *η* for both structures in "7.84 cm^2" and "3.92 cm^2" cell designs. Note that the cells do not have a double-antireflection-layers on the front to even more clearly show the transparency of our n-type contact stack. Eventually, cells with both front and rear junction structures achieved *η* of around 22.0%. Furthermore, to clarify the advantage of using (n)nc-SiO$_x$:H contact stack over (n)a-Si:H layer, the J-V parameters and EQE curves of two rear junction cell designs with either combined 8 nm (n)nc-SiO$_x$:H–2 + 3 nm (n)nc-Si:H + 2 nm (n)a-Si:H layer stack or only 6 nm (n)a-Si:H are compared and given in Table 4 and Figure 8, respectively.

From Table 4, it is obvious that an average gain of 1.5 mA/cm^2 in J_{SC} results in an average improved efficiency of 0.8%$_{abs}$ when (n)nc-SiO$_x$:H contact stack is applied. Specifically, the EQE curves given in Figure 8 reveal that by using (n)nc-SiO$_x$:H layer stack, the cell has significantly enhanced EQE till 650 nm and slightly improved EQE from 1000 nm.

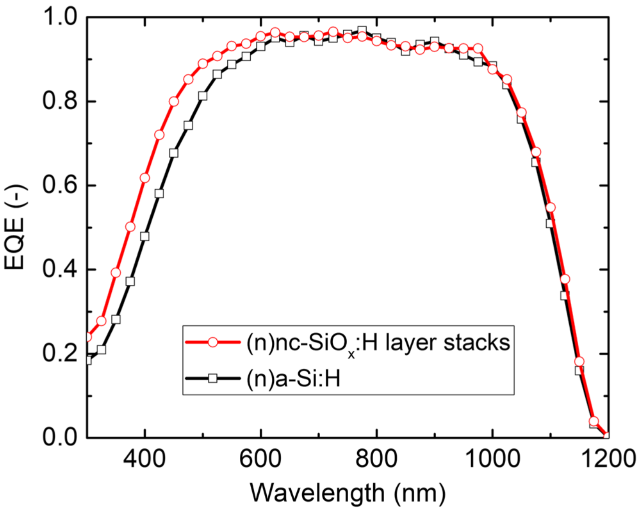

FIGURE 8 The external quantum efficiency (EQE) curves of rear junction cells with only 6 nm (n)a-Si:H layer and 8 nm (n)nc-SiO$_x$:H–2 + 3 nm (n)nc-Si:H + 2 nm (n)a-Si:H layer stack [Colour figure can be viewed at wileyonlinelibrary.com]

Even though transport mechanisms have been unveiled for achieving ultimate *FF* in SHJ cells,[6] the pre-conditioning for optimal layer's growth and other experimental steps, such as pre- and post-treatments as well as back end metallization, heavily impact on the road towards ultimate transport. In fact, the notable difference between *pFF* and *FF* shown in Table 3 indicates further optimizations are required to minimize the transport resistivity of charge carriers. In this respect, a measurement of the contact resistance between doped contact-stacks and TCO layers based on transfer length method would give more insights.

Additional optimizations of TCO and front metal grids are required for improving further the cell efficiency. It is expected that solar cells with mainly doped nc-SiO$_x$:H and nc-Si:H contact stacks, combined with (a) wafers thinner than approximately 280 μm, (b) even lower metallization fraction, and (c) novel TCOs, such as hydrogenated fluorine-doped indium oxide,[55] will enable efficiency well beyond 23% without dual antireflective coating. Moreover, we also expect that doped nc-Si (O$_x$):H layers deposited under VHF will deliver better layer and cell performances than layers deposited under RF. Besides, this SHJ cell will be further optimized for application in the perovskite/crystalline silicon tandem solar cell.

4 | CONCLUSIONS

In this study, we developed transparent carrier-selective transport layers mainly based on nc-SiO$_x$:H alongside with interface treatments to improve carrier collection in SHJ applications.

Nc-SiO$_x$:H layers with state-of-the-art electrical properties (σ_{dark} = 1.02 S/cm for n-type and 0.04 S/cm for p-type) and optical properties (n = 2.13 and E_{04} = 2.96 eV for n-type) are achieved and used in solar cells. We observed improved electrical properties

(E_a and σ_{dark}) of test structures after pre-treatments (pre-HPT, non-oxidic nc-Si:H seed layer and VHF (i)nc-Si:H) and also excellent passivation on c-Si/(i)a-Si:H interface with τ_{eff} over 11 ms when combined pre-HPT and VHF (i)nc-Si:H treatments is applied. The post-treatments, especially 2 nm of (n)a-Si:H and (p)a-Si:H capping layer applied on n-type and p-type contact stacks, respectively, demonstrate significant improvements on σ_{dark} from 0.79 to 2.03 S/cm for n-type contact stacks and from 0.02 to 0.07 S/cm for p-type contact stacks. Eventually, we implemented the interface treatments into front/back-contacted silicon heterojunction solar cells giving a guideline for nanocrystalline film development. We monitored the *FF* and V_{OC} to evaluate the effects of different treatments, which affect the nucleation of doped layers and their interface with ITO. Combining optimized interface treatments on the contact stacks, we improve the *FF* from 65.6% in a rear junction cell to 77.9% in a front junction cell (7.84 cm^2). Furthermore, cells with area of 3.92 cm^2 featuring 4.4% metal coverage demonstrate improvement of *FF* from 77.9% to 79.1% and 75.3% to 78.6%, thus η from 18.4% to 21.8% and 18.3% to 22.0% are achieved for front and rear junction cells, respectively, with perspective of further improvements by optimizing the front grid, bulk thickness and using more transparent TCO.

ACKNOWLEDGEMENT

This study receives financial support from the NWO Joint Solar Program III (680-91-011) and technical support from PVMD group technicians Martijn Tijssen and Stefaan Heirman.

REFERENCES

1. Adachi D, Hernández JL, Yamamoto K. Impact of carrier recombination on fill factor for large area heterojunction crystalline silicon solar cell with 25.1% efficiency. *Appl Phys Lett*. 2015;107(23):233506.
2. Yoshikawa K, Kawasaki H, Yoshida W, et al. Silicon heterojunction solar cell with interdigitated back contacts for a photoconversion efficiency over 26%. *Nat Energy*. 2017;2(5):17032.
3. Masuko K, Shigematsu M, Hashiguchi T, et al. Achievement of more than 25% conversion efficiency with crystalline silicon heterojunction solar cell. *IEEE J Photovoltaics*. 2014;4(6):1433-1435.
4. Yoshikawa K, Yoshida W, Irie T, et al. Exceeding conversion efficiency of 26% by heterojunction interdigitated back contact solar cell with thin film Si technology. *Sol Energy Mater Sol Cells*. 2017;173:37-42.
5. Herasimenka SY, Dauksher WJ, Bowden SG. >750 mV open circuit voltage measured on 50 μ m thick silicon heterojunction solar cell. *Appl Phys Lett*. 2013;103(5):053511.
6. Procel P, Yang G, Isabella O, Zeman M. Theoretical evaluation of contact stack for high efficiency IBC-SHJ solar cells. *Sol Energy Mater Sol Cells*. 2018;186:66-77.
7. Holman ZC, Descoeudres A, Barraud L, et al. Current losses at the front of silicon heterojunction solar cells. *IEEE J Photovoltaics*. 2012;2(1):7-15.
8. Rehm W, Fischer R, Stuke J, Wagner H. Photo and dark conductivity of doped amorphous silicon. *Phys status solidi*. 1977;79(2):539-547.
9. De Wolf S, Kondo M. Boron-doped a-Si:Hc-Si interface passivation: degradation mechanism. *Appl Phys Lett*. 2007;91(11):112109.
10. Xu Y, Hu Z, Diao H, et al. Heterojunction solar cells with n-type nanocrystalline silicon emitters on p-type c-Si wafers. *J Non Cryst Solids*. 2006;352(9):1972-1975.
11. Seif JP, Descoeudres A, Nogay G, et al. Strategies for doped nanocrystalline silicon integration in silicon heterojunction solar cells. *IEEE J Photovoltaics*. 2016;6(5):1132-1140.
12. Nogay G, Seif JP, Riesen Y, et al. Nanocrystalline silicon carrier collectors for silicon heterojunction solar cells and impact on low-temperature device characteristics. *IEEE J Photovoltaics*. 2016;6(6):1654-1662.
13. Martins R, Macarico A, Ferreira I, et al. Highly conductive and highly transparent n-type microcrystalline silicon thin films. *Thin Solid Films*. 1997;303(1–2):47-52.
14. Keblinski P, Phillpot SR, Wolf D, Gleiter H. Amorphous structure of grain boundaries and grain junctions in nanocrystalline silicon by molecular-dynamics simulation. *Acta Mater*. 1997;45(3):987-998.
15. Vetterl O, Finger F, Carius R, et al. Intrinsic microcrystalline silicon: a new material for photovoltaics. *Sol Energy Mater Sol Cells*. 2000;62(1–2):97-108.
16. Cuony P, Alexander DTL, Perez-Wurfl I, et al. Silicon filaments in silicon oxide for next-generation photovoltaics. *Adv Mater*. 2012;24(9):1182-1186.
17. Mazzarella L, Morales-Vilches AB, Hendrichs M, et al. Nanocrystalline n-type silicon oxide front contacts for silicon heterojunction solar cells: photocurrent enhancement on planar and textured substrates. *IEEE J Photovoltaics*. 2017;8(1):70-78.
18. Lambertz A, Smirnov V, Merdzhanova T, et al. Microcrystalline silicon–oxygen alloys for application in silicon solar cells and modules. *Sol Energy Mater Sol Cells*. 2013;119:134-143.
19. Richter A, Smirnov V, Lambertz A, Nomoto K, Welter K, Ding K. Versatility of doped nanocrystalline silicon oxide for applications in silicon thin-film and heterojunction solar cells. *Sol Energy Mater Sol Cells*. 2018;174:196-201.
20. Sritharathikhun J, Yamamoto H, Miyajima S, Yamada A, Konagai M. Optimization of amorphous silicon oxide buffer layer for high-efficiency p-type hydrogenated microcrystalline silicon oxide/n-type crystalline silicon heterojunction solar cells. *Jpn J Appl Phys*. 2008;47(11R):8452-8455.
21. Mazzarella L, Kirner S, Stannowski B, Korte L, Rech B, Schlatmann R. p-type microcrystalline silicon oxide emitter for silicon heterojunction solar cells allowing current densities above 40 mA/cm2. *Appl Phys Lett*. 2015;106(2):23902.
22. Nakada K, Miyajima S, Konagai M. Application of n-type microcrystalline silicon oxide as back reflector of crystalline silicon heterojunction solar cells. *Jpn J Appl Phys*. 2015;54(8):82301.
23. Roca i Cabarrocas P, Layadi N, Heitz T, Drévillon B, Solomon I. Substrate selectivity in the formation of microcrystalline silicon: mechanisms and technological consequences. *Appl Phys Lett*. 1995;66(26):3609-3611.
24. Koh J, Fujiwara H, Koval RJ, Wronski CR, Collins RW. Real time spectroscopic ellipsometry studies of the nucleation and growth of p-type microcrystalline silicon films on amorphous silicon using B2H6, B(CH3)3 and BF3 dopant source gases. *J Appl Phys*. 1999;85(8):4141-4153.
25. Pellaton Vaucher N, Rech B, Fischer D, et al. Controlled nucleation of thin microcrystalline layers for the recombination junction in a-Si stacked cells. *Sol Energy Mater Sol Cells*. 1997;49(1–4):27-33.
26. Wolff J, Carius R, Finger F. Preparation of microcrystalline silicon seed-layers with defined structural properties. *Thin Solid Films*. 2003;427:46-50.
27. Zhou J, Ikuta K, Yasuda T, et al. Growth of amorphous-layer-free microcrystalline silicon on insulating glass substrates by plasma-enhanced chemical vapor deposition. *Appl Phys Lett*. 2003;1534(1997):1-4.
28. Mazzarella L, Kirner S, Gabriel O, et al. Nanocrystalline silicon emitter optimization for Si-HJ solar cells: substrate selectivity and CO2 plasma treatment effect. *Phys Status Solidi Appl Mater Sci*. 2017;214(2):1532958.

29. Mews M, Schulze TF, Mingirulli N, Korte L. Hydrogen plasma treatments for passivation of amorphous-crystalline silicon-heterojunctions on surfaces promoting epitaxy. *Appl Phys Lett*. 2013;102(12):122106.
30. Descoeudres A, Barraud L, De Wolf S, et al. Improved amorphous/-crystalline silicon interface passivation by hydrogen plasma treatment. *Appl Phys Lett*. 2011;99(12):1-4.
31. Pangal K, Sturm JC, Wagner S, Büyüklimanli TH. Hydrogen plasma enhanced crystallization of hydrogenated amorphous silicon films. *J Appl Phys*. 1999;85(3):1900-1906.
32. Dutta J, Kroll U, Chabloz P, et al. Dependence of intrinsic stress in hydrogenated amorphous silicon on excitation frequency in a plasma-enhanced chemical vapor deposition process. *J Appl Phys*. 1992;72(7):3220-3222.
33. Finger F, Hapke P, Luysberg M, Carius R, Wagner H, Scheib M. Improvement of grain size and deposition rate of microcrystalline silicon by use of very high frequency glow discharge. *Appl Phys Lett*. 1994;65(20):2588-2590.
34. Tan H, Babal P, Zeman M, Smets AHM. Solar Energy materials & solar cells wide bandgap p-type nanocrystalline silicon oxide as window layer for high performance thin- fi lm silicon multi-junction solar cells. *Sol Energy Mater Sol Cells*. 2015;132:597-605.
35. WTheiss Hardware and Software. SCOUT.
36. Yang G, Guo P, Procel P, et al. High-efficiency black IBC c-Si solar cells with poly-Si as carrier-selective passivating contacts. *Sol Energy Mater Sol Cells*. 2018;186:9-13.
37. Deligiannis D, Alivizatos S, Ingenito A, et al. Wet-chemical treatment for improved surface passivation of textured silicon heterojunction solar cells. *Energy Procedia*. 2014;55:197-202.
38. Olibet S, Monachon C, Hessler-Wyser A, et al. Textured silicon heterojunction solar cells with over 700 mV open-circuit voltage studied by transmission electron microscopy. *23rd EUPVSEC*. 2008
39. Lambertz A, Grundler T, Finger F. Hydrogenated amorphous silicon oxide containing a microcrystalline silicon phase and usage as an intermediate reflector in thin-film silicon solar cells. *J Appl Phys*. 2011;109(11):113109.
40. Gabriel O, Kirner S, Klingsporn M, Friedrich F, Stannowski B, Schlatmann R. On the plasma chemistry during plasma enhanced chemical vapor deposition of microcrystalline silicon oxides. *Plasma Processes Polym*. 2015;12(1):82-91.
41. Richter A, Zhao L, Finger F, Ding K. Nano-composite microstructure model for the classification of hydrogenated nanocrystalline silicon oxide thin films. *Surf Coat Technol*. 2016;295:119-124.
42. Kirner S, Neubert S, Schultz C, et al. Quadruple-junction solar cells and modules based on amorphous and microcrystalline silicon with high stable efficiencies. *Jpn J Appl Phys*. 2015;54(8S1):08 KB03.
43. Matsuda A. Formation kinetics and control of microcrystallite in μc-Si:H from glow discharge plasma. *J Non Cryst Solids*. 1983;59-60(PART 2):767-774.
44. Kondo M, Fukawa M, Guo L, Matsuda A. High rate growth of microcrystalline silicon at low temperatures. *J Non Cryst Solids*. 2000;266–269:84-89.
45. Cuony P, Marending M, Alexander DTL, et al. Mixed-phase p-type silicon oxide containing silicon nanocrystals and its role in thin-film silicon solar cells. *Appl Phys Lett*. 2010;97(21):213502.
46. Kaiser I, Nickel NH, Fuhs W. Hydrogen-mediated structural changes of amorphous and microcrystalline silicon. *Phys Rev B*. 1998;58(4):1718-1721.
47. Nunomura S, Sakata I, Matsubara K. In-situ detection of interface defects in a-Si:H/c-Si heterojunction during plasma processing. *Appl Phys Express*. 2019;12(5):51006.
48. Beyer W, Ghazala MSA. Absorption strengths of Si-H vibrational modes in hydrogenated silicon. *MRS Online Proc Libr Arch*. 1998;507.
49. Lucovsky G, Nemanich RJ, Knights JC. Structural interpretation of the vibrational spectra of a-Si:H alloys. *Phys Rev B*. 1979;19(4):2064.
50. Ziegler Y, Daudrix V, Droz C, Platz R, Wyrsch N, Shah A. More stable low gap a-Si: H layers deposited by PE-CVD at moderately high temperature with hydrogen dilution. *Sol Energy Mater Sol Cells*. 2001;66(1–4):413-419.
51. Roca i Cabarrocas P, Layadi N, Drevillon B, Solomon I. Microcrystalline silicon growth by the layer-by-layer technique: long term evolution and nucleation mechanisms. *J Non Cryst Solids*. 1996;198-200:871-874.
52. Sheng S, Hao H, Diao H, et al. XPS depth profiling study of n/TCO interfaces for p-i-n amorphous silicon solar cells. *Appl Surf Sci*. 2006;253(3):1677-1682.
53. Gao M, Wan Y, Li Y, et al. Effective passivation and tunneling hybrid a-SiO$_x$(In) layer in ITO/n-Si heterojunction photovoltaic device. *ACS Appl Mater Interfaces*. 2017;9(20):17565-17575.
54. Klein A, Körber C, Wachau A, et al. Transparent conducting oxides for photovoltaics: manipulation of fermi level,work function and energy band alignment. *Materials (Basel)*. 2010;3(11):4892-4914.
55. Han C, Mazzarella L, Zhao Y, et al. High-mobility hydrogenated fluorine-doped indium oxide film for passivating contacts c-Si solar cells. *ACS Appl Mater Interfaces*. 2019;11(49):45586-45595.

How to cite this article: Zhao Y, Mazzarella L, Procel P, et al. Doped hydrogenated nanocrystalline silicon oxide layers for high-efficiency c-Si heterojunction solar cells. *Prog Photovolt Res Appl*. 2020;1–11. https://doi.org/10.1002/pip.3256